

## MOLECULAR BIOLOGY

## Structural basis of autoinhibition of the human NHE3-CHP1 complex

Yanli Dong<sup>1,2†</sup>, Hang Li<sup>1,2†</sup>, Alina Ilie<sup>3†</sup>, Yiwei Gao<sup>1,2</sup>, Annie Boucher<sup>3</sup>, Xuejun Cai Zhang<sup>1\*</sup>, John Orlowski<sup>3\*</sup>, Yan Zhao<sup>1\*</sup>

Sodium-proton exchanger 3 (NHE3/SLC9A3) located in the apical membrane of renal and gastrointestinal epithelia mediates salt and fluid absorption and regulates pH homeostasis. As an auxiliary regulatory factor of NHE proteins, calcineurin B homologous protein 1 (CHP1) facilitates NHE3 maturation, plasmalemmal expression, and pH sensitivity. Dysfunctions of NHE3 are associated with renal and digestive system disorders. Here, we report the cryo-electron microscopy structure of the human NHE3-CHP1 complex in its inward-facing conformation. We found that a cytosolic helix-loop-helix motif in NHE3 blocks the intracellular cavity formed between the core and dimerization domains, functioning as an autoinhibitory element and hindering substrate transport. Furthermore, two phosphatidylinositol molecules are found to bind to the peripheric juxtamembrane sides of the complex, function as anchors to stabilize the complex, and may thus enhance its transport activity.

## INTRODUCTION

$\text{Na}^+/\text{H}^+$  exchangers or antiporters (NHEs/NHAs) are integral membrane secondary active transporters present in all living organisms examined to date, giving credence to the notion that they originated during the earliest stages of biosphere evolution (1). Their universal evolutionary conservation suggests that they played a vital role in the emergence of primordial life forms from primitive protocells. It has been postulated that NHEs served initially as a bioenergetic feedback loop. In such a system, NHEs sustain chemiosmotic coupling of geochemical-generated  $\text{H}^+$  gradients to ion gradient-harnessing adenosine triphosphate (ATP) synthases responsible for energy production that fueled the development of autonomous life forms (1). Concomitant with increasing species complexity and diversification, these solute carriers expanded genetically to accommodate additional functions and now constitute a monovalent cation-proton antiporter (CPA) superfamily consisting of two major branches, i.e., CPA1 (electroneutral) and CPA2 (electrogenic). For mammals, the CPA superfamily contains 13 CPAs encoded by the solute carrier 9 (SLC9) gene family. These transporters display various tissue distribution, subcellular localization, cation selectivity, physiological functions, and regulation in response to diverse stimuli (2, 3). As one of the well-studied NHE prototypes, human NHE3 (SLC9A3) plays key roles in salt and fluid absorption and pH homeostasis. It is expressed predominantly in the renal and digestive systems, specifically the microvillar membranes and subapical recycling endosomes of renal, gastrointestinal, and gallbladder epithelia. Genetic ablation of NHE3 in mice causes mild diarrhea, proximal tubular acidosis, and hypotension (4). Dysregulation of NHE3 activity has also been implicated in several human disease conditions, including cholestasis (5), cholesterol gallstone (6), cystic fibrosis (7), ulcerative colitis (8), Crohn's disease (9), and congenital sodium diarrhea (10).

Molecular mechanisms of NHE proteins and their bacterial homologs (e.g., Nha or Nap) have been studied extensively over the past

two decades. Recently, mammalian NHE1 and NHE9 structures have been reported (11, 12). These studies revealed that NHE-like transporters typically assemble as homodimers, with each protomer having 13 transmembrane (TM) helices. These helices further form a dimerization domain (TMs 1 to 3 and 8 to 10) and a core domain (TMs 4 to 6 and 11 to 13) with a long linker helix (TM7) in between. In each protomer, the ion translocation pore is located between the two domains with highly conserved acidic residues clustered halfway across the lipid bilayer. These negatively charged residues are involved in cation binding and are alternately exposed to the intracellular and extracellular sides of the membrane during the transport cycle (11, 13–15). An elevator-like transport model has been proposed for CPA homologs based on structural analyses of both inward- and outward-facing conformations (16, 17).

The activities of NHEs are regulated by a variety of auxiliary proteins. For instance, NHE1 and NHE3 are known to bind calcineurin B homologous protein 1 (CHP1) with nanomolar affinity, which facilitates the maturation, cell surface expression, and function of the transporters (18). Our previous human NHE1-CHP1 complex structure reveals the binding mode between NHE1 and CHP1 (11). The mechanisms underlying activity regulation are not fully resolved but are thought to involve a switch between active and inactive (autoinhibition) modes in response to various stimuli (19–21). In addition, NHE1 and NHE3 are activated directly or indirectly by membrane phosphoinositides (PIs), such as phosphorylated phosphatidylinositol (PtdIns) derivatives  $\text{PtdIns}(4,5)\text{P}_2$  and  $\text{PtdIns}(3,4,5)\text{P}_3$  (22–25), yet these properties remain to be explained structurally. In the present work, we report the human NHE3-CHP1 complex structure in its autoinhibitory conformation. In addition to providing insight into the molecular mechanism of autoinhibition, we have also identified a pair of PI binding sites in the complex, which may allow us to refine the elevator model of NHE-like transporters.

## RESULTS AND DISCUSSION

## Regulation of the NHE3 by CHP1

To determine the regulatory role of CHP1 on NHE3 function, cultured Chinese hamster ovary AP-1 cells were transfected with a plasmid encoding either NHE3 tagged at its C terminus with mCherry fluorescent

Copyright © 2022  
The Authors, some  
rights reserved;  
exclusive licensee  
American Association  
for the Advancement  
of Science. No claim to  
original U.S. Government  
Works. Distributed  
under a Creative  
Commons Attribution  
NonCommercial  
License 4.0 (CC BY-NC).

Downloaded from https://www.science.org on April 09, 2025

<sup>1</sup>National Laboratory of Biomacromolecules, CAS Center for Excellence in Biomacromolecules, Institute of Biophysics, Chinese Academy of Sciences, Beijing 100101, China. <sup>2</sup>College of Life Sciences, University of Chinese Academy of Sciences, Beijing 100049, China. <sup>3</sup>Department of Physiology, McGill University, Montreal, Canada.

\*Corresponding author. Email: zhangc@ibp.ac.cn (X.C.Z.); john.orkowski@mcgill.ca (J.O.); zhaoy@ibp.ac.cn (Y.Z.)

†These authors contributed equally to this work.

protein (ChFP) (abbreviated simply as NHE3) alone or the NHE3-CHP1 complex. The AP-1 cells are a mutagenized cell line devoid of plasma membrane  $\text{Na}^+/\text{H}^+$  exchange activity (26), thereby allowing unambiguous assessment of NHE3 function. Previous studies have shown that NHE3 resides not only on the cell surface but also in recycling endosomes when expressed endogenously in epithelial cells (27) or exogenously in epithelial (28) and nonepithelial cells (29). To accurately evaluate the effect of CHP1 on NHE3 abundance and subcellular distribution, NHE3 and CHP1 protein expression was biochemically assessed in both total cell lysates and at the plasma membrane (plasmalemmal proteins were extracted using a cell surface biotinylation protocol) by Western blotting and quantified by densitometry. To correct for protein loading, the ratio of surface/total NHE3 expression was normalized to  $\beta$ -tubulin. Expression of endogenous plasmalemmal  $\text{Na}^+/\text{K}^+$ -adenosine triphosphatase (ATPase)  $\alpha 1$  subunit (ATP1A1) was also determined to validate the biotinylation assay to selectively extract surface-resident proteins.

The results showed that coexpression of CHP1 not only stabilized and consequently increased the total cellular level of NHE3 but also led to a net increase (approximately two- to fourfold) in the surface abundance of NHE3 and CHP1 relative to NHE3 alone (Fig. 1, A and B). Low levels of endogenous CHP1 were detected in AP-1 cell lysates, a finding consistent with the low surface expression of exogenous NHE3 in the absence of sufficient CHP1. The enhanced surface expression of NHE3 in the presence of CHP1 was corroborated visually by fluorescence confocal microscopy (Fig. 1C). As expected, a substantial fraction of NHE3, regardless of the presence or absence of CHP1, also resided mainly in perinuclear vesicles labeled with transferrin-Alexa Fluor 488 (Tf-Alexa<sup>488</sup>), a marker of both fast (peripheral) and slow (perinuclear) recycling endosomes (30). To determine whether the CHP1-mediated elevation of NHE3 surface expression also resulted in a corresponding increase in transport activity, plasmalemmal NHE3 function was evaluated by measuring the initial rates of external  $\text{Na}^+$ -dependent recovery of cytosolic pH following

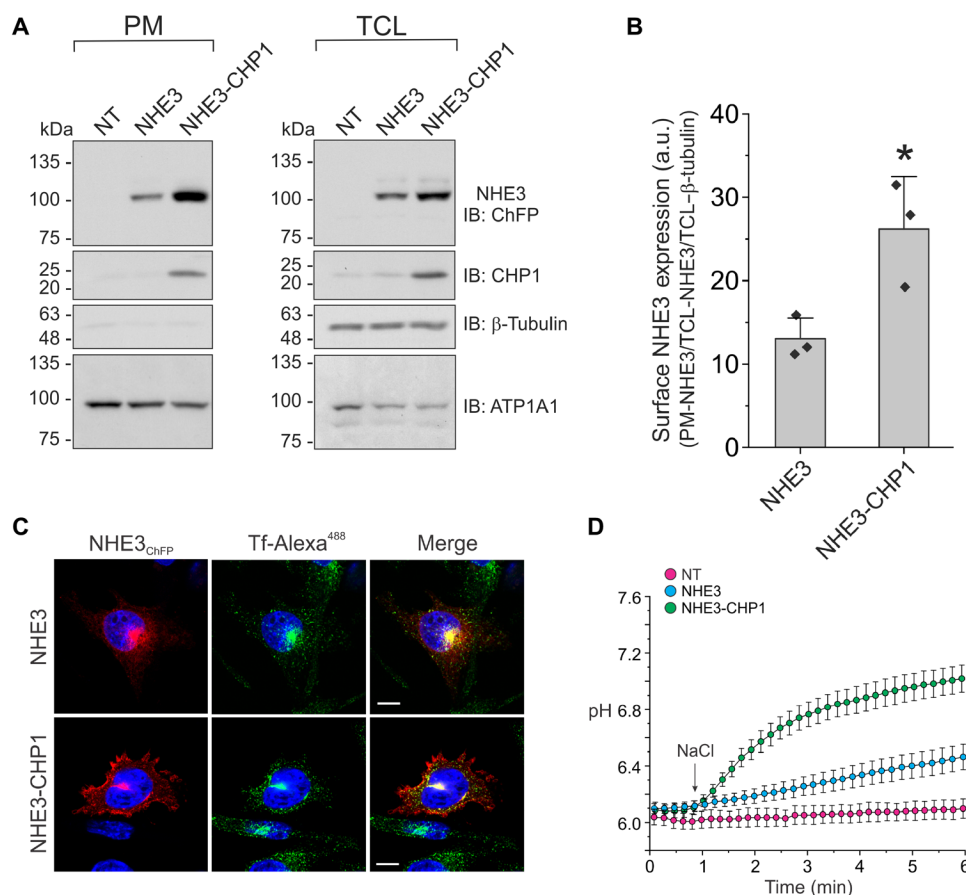


**Fig. 1. Regulation of the NHE3 by CHP1.** (A) Biochemical assessment of NHE3 protein expression and membrane trafficking. Chinese hamster ovary AP-1 cells were transiently transfected with a single plasmid encoding either mCherry fluorescent protein [ChFP; no transporter (NT)], NHE3, or NHE3-CHP. Total cell lysates (TCLs; 40  $\mu$ g of protein per lane) and plasma membrane (PM) fractions (1 mg of protein per lane) were analyzed by Western blotting using mouse monoclonal antibodies to detect ChFP (NHE3), CHP1,  $\beta$ -tubulin, and ATP1A1 ( $\text{Na}^+/\text{K}^+$ -ATPase 1 subunit).  $\beta$ -Tubulin and ATP1A1 served as loading controls for TCL and PM fractions, respectively. (B) Densitometric quantification of the surface abundance of NHE3 in the absence or presence of CHP1 was normalized to the total cellular expression of NHE3 and  $\beta$ -tubulin. Data are shown as means  $\pm$  SD of three separate experiments. Statistical significance was assessed using the unpaired two-sample *t* test; \**P* < 0.05. (C) Immunofluorescence of AP-1 cells transiently transfected with NHE3 or NHE3-CHP1. Nuclei were labeled with DNA dye 4',6-diamidino-2-phenylindole. Images show each channel individually, with merged images of the NHE3 and Tf-Alexa<sup>488</sup> channels. Scale bars, 10  $\mu$ m. Images are representative of two independent experiments. (D) NHE3 activity was assessed by measuring cytoplasmic pH recovery following an  $\text{NH}_4^+$ -induced acid load in AP-1 cells transfected with ChFP (NT), NHE3, or NHE3-CHP1. Recovery of pH was initiated by addition of an isotonic  $\text{Na}^+$ -rich solution (indicated by an arrow). Tracings are average values (means  $\pm$  SEM) from three to five cells and representative of at least two independent experiments.

an  $\text{NH}_4\text{Cl}$ -induced intracellular acidification [pH was assessed using the ratiometric fluorophore BCECF (2',7'-bis-(carboxyethyl)-5-(and-6)-carboxyfluorescein)] of ChFP-labeled cells. As anticipated, the increased surface protein expression of NHE3-CHP1 correlated with an  $\approx 4.6$ -fold increase in transport activity relative to NHE3 alone (Fig. 1D). These findings indicate that CHP1 promotes not only the stabilization of NHE3 but also its trafficking and activity at the plasma membrane.

### Architecture of the NHE3-CHP1 complex

To gain insights into how CHP1 regulates NHE3, the NHE3-CHP1 protein complex was purified and reconstituted into a nanodisc (fig. S1, A to C). Subsequently, single-particle cryo-electron microscopy (cryo-EM) studies were performed, which resolved the complex structure at 3.2 Å (figs. S2, A to D and S3 and table S1). The resulting model reveals that human NHE3 assembles as a homodimer, with each protomer consisting of 834 amino acid residues that fold into a 13-helix TM domain (TMD; residues 40 to 465), a short extracellular N-terminal region, and a long cytoplasmic C-terminal tail (Fig. 2, A and B). The first 39 residues are missing in our structure, which is consistent with a previous study indicating that the NHE3 has a cleavable signal peptide (31). No N-glycans were determined

in our cryo-EM map. The twofold symmetry axis relating the two protomers is perpendicular to the membrane plane. In terms of local symmetry, the N-terminal half of TMD (TMs 1 to 6, i.e., half of the dimerization domain together with half of the core domain) is related to the C-terminal half (TMs 8 to 13) through a pseudo-twofold symmetry with the rotation axis parallel to the membrane plane. Each protomer is composed of two distinct domains, i.e., the thinner dimerization domain in the central region of the NHE3 dimer and the thicker core domain at one end of the elongated dimer (Fig. 2, C and D), consistent with previously reported NHE-like structures, including prokaryotic *Thermus thermophilus* NapA (*Tt*NapA) (17), *Pyrococcus abyssi* NhaP (*Pa*NhaP) (15), *Methanocaldococcus jannaschii* NhaP (*Mj*NhaP) (14), eukaryotic *Homo sapiens* NHE1 (*Hs*NHE1) (11), and *Equus caballus* (horse) NHE9 (*Eca*NHE9) (12).

In the current structure, residues 40 to 665 are well resolved and modeled, whereas the terminal parts are missing presumably because of their structural flexibility. The missing parts also include the linking regions between the TMD and the C-terminal helical segment HC1 and between HC3 and HC4. The overall structure of the NHE3-CHP1 complex appears as a crab shape with a TMD body and two attached CHP1 chelipeds ("legs") positioned on the cytoplasmic side (Fig. 2A). Taking a closer look at TMD, the dimer

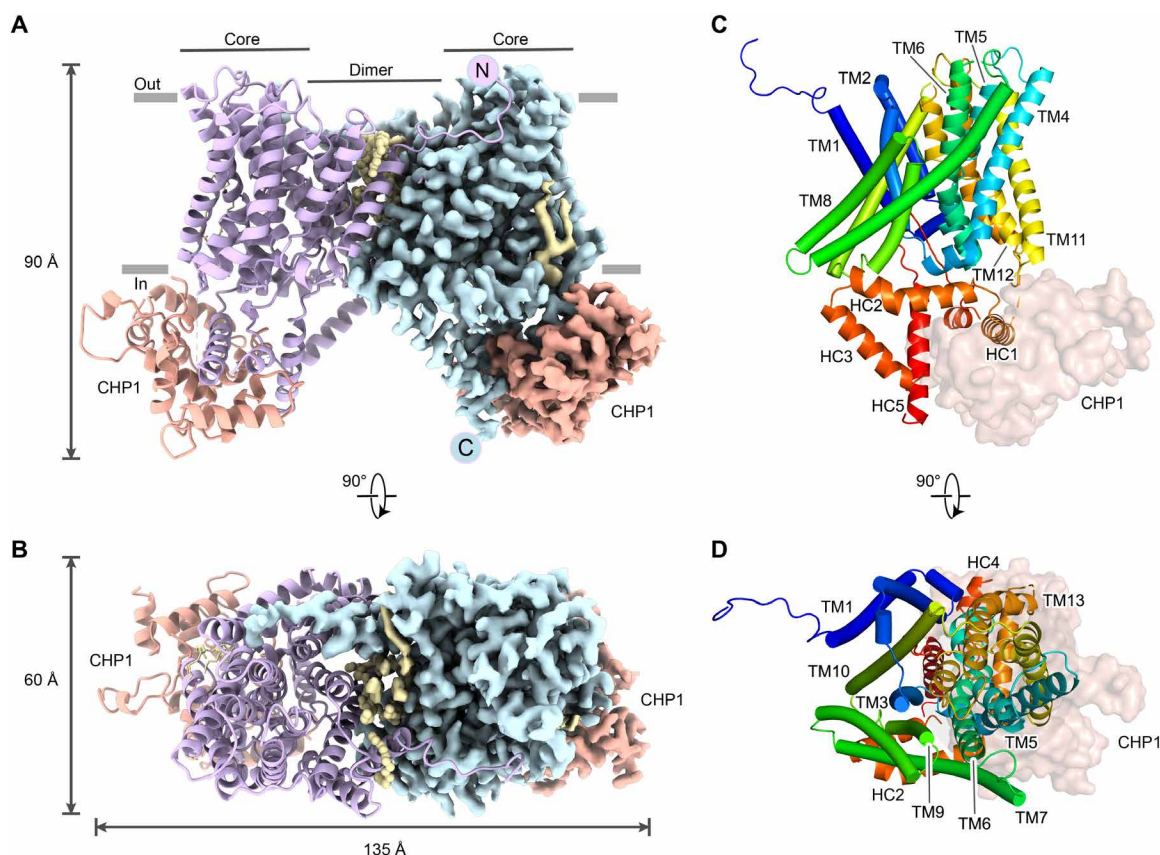


**Fig. 2. Architecture of the NHE3-CHP1 complex.** (A and B) Overall structure of the NHE3-CHP1 complex. NHE3 subunits from either model (left) or EM map (right) are combined and colored in violet and blue. Two CHP1 subunits are displayed in the same way and shown in salmon color. The bound lipids are colored in yellow. The N and C termini of NHE3 are labeled. Gray bars represent boundaries of the cell membrane, and the dimensions of the complex (135 Å by 60 Å by 90 Å) are marked. (C and D) Structure of the NHE3 protomer viewed in the membrane plane and from the extracellular side. The peptide backbone of NHE3 is colored in a rainbow scheme, with blue and red for the N and C termini, respectively. The core and dimerization domains are shown in cartoon and cylinder, respectively. The CHP1 molecule is displayed as a transparent orange surface model. The core domain is highlighted with a gray oval in the top view.



interface is formed by TMs 1, 3, 8, and 10 from both protomers and results in a hydrophobic cavity open to the extracellular side, which is filled with several lipid molecules with different degrees of density integrity (Fig. 2B and fig. S3). We speculate that these lipids are critical for dimerization of the NHE3 and might regulate movement of the dimerization and the core domains relative to the membrane plane in the NHE3 transport cycle (32). The NHE3 protomer structure has an inward-facing conformation with the ligand-binding cavity made up of TMs 2, 3, 5, 6, 10, and 12. Inside the cavity, the broken helix TM5, together with TM6, contributes to the formation of the substrate-binding site (fig. S4).

Beyond TMD, the region C-terminal to TM13 in each protomer extends into the cytoplasm, forming five helices, HC1 to HC5, along with other mostly missing regions. Multiple residues of HC1 bind to the bottom of a hydrophobic cleft formed by the N- and C-lobes of CHP1 by hydrophobic matching (fig. S5A). The complementary size and shape of this crevice together with contacts between polar noncharged amino acids assure a high degree of interaction specificity with HC1 (33). For instance, H480 in HC1 ( $\text{H480}^{\text{HC1}}$ ) of NHE3 not only forms polar interaction with the hydroxyl group of  $\text{Y122}^{\text{CHP1}}$  but also interacts with the benzene rings from both  $\text{Y122}^{\text{CHP1}}$  and  $\text{F176}^{\text{CHP1}}$  through  $\pi$ - $\pi$  packing (fig. S5B). This set of favorable interactions imply that  $\text{H480}^{\text{HC1}}$  plays a key role in specific interaction with CHP1. C-terminal to HC1, the amphipathic HC2 presumably binds to the membrane surface (Fig. 2C). In addition, HC3 forms approximately  $45^\circ$  angle with the horizontal HC2, protruding to the cytosol. Because HC3 and HC4 are far apart, their missing connection loop is composed of 79 residues and likely assumes an extended conformation. It is not clear whether HC4 swapping occurs between the two protomers.

Structural comparison of the human NHE3-CHP1 complex with the inward-facing NHE1-CHP1 complex reveals no significant difference in protomer TMD (including HC2 but not HC1) with a root mean square deviation of  $1.5 \text{ \AA}$  for 434 Ca pairs (fig. S6, A, B and D), indicating that the NHE3-CHP1 complex is stabilized at an inward-facing conformation. However, relative displacement of HC1-bound CHP1 subunits reaches  $11 \text{ \AA}$ , estimated based on the center of mass of the corresponding CHP1 subunits. In addition, there is an apparent  $14^\circ$  rotation between the CHP1 subunits of the NHE1- and NHE3-CHP1 complexes (fig. S6C), reflecting the flexibility of CHP1 binding in the inward-facing conformation (11). Comparing structures of the NHE1-CHP1 and NHE3-CHP1 complexes at either inward- or outward-facing conformation, we found that the HC1 associating with CHP1 exhibits substantial conformational heterogeneity. However, the amphipathic helix HC2 is similarly positioned relative to the TMD and floats on the membrane. We speculate that their distinct behaviors in conformational change relative to the TMD are critical for the regulation roles of CHP1 or activity of NHE1/NHE3.

The inward-facing substrate-binding cavity is  $\sim 17 \text{ \AA}$  in depth and has an estimated  $250\text{-}\text{\AA}^3$  volume. Its inner surface appears to be electronegative due to distribution of acidic residues halfway across the membrane. As illustrated in the *PaNhaP* crystal structural and confirmed by functional studies, a thallium ion can serve as a ligand and binds these acidic residues during transport (15). By structural comparison, we identified the corresponding residues potentially responsible for  $\text{Na}^+$  binding in NHE3: the side chains of S217 and D221, backbone carbonyl of V191, and a water molecule coordinated by D192 jointly bind one  $\text{Na}^+$  ion. Among them, D221 is likely to be

the main candidate for protonation, which competes with  $\text{Na}^+$  binding. Notably, in the absence of a substrate  $\text{Na}^+$ , the side chain of S217 does not orient toward the putative ion position (fig. S4B).

### Autoinhibitory mechanism of the NHE3

HC4, HC5, and their connecting loop in the cytosolic tail of NHE3 form a hairpin structure, the tip of which inserts into the above-mentioned inward-facing cavity of the NHE3 protomer. This special functional motif is referred to as a plug motif, reflecting its lock-and-key interaction mode with the cavity (Fig. 3A and fig. S4A). The plug-like HC4-loop-HC5 motif in NHE3 (residues 617 to 665; also referred to as HLH motif) consists of HC4 (residues H618 to Y623), HC5 (E644 to S663), and the loop in between (L624 to T643). The loop region in this motif folds into a hairpin shape and plugs into the inward-facing cavity of NHE3. This loop insertion extends all the way up to the inner surface formed by the middle residues of TM10 (Fig. 3A). This binding buries approximately  $4870 \text{ \AA}^2$  of solvent-accessible surface in the interface between each HLH motif and the remaining part of the NHE3-CHP1 complex, in which approximately  $870 \text{ \AA}^2$  comes from TMD,  $1380 \text{ \AA}^2$  from the CHP1 and the cytosolic region of NHE3, and  $2620 \text{ \AA}^2$  from the HLH motif. Interactions stabilizing this previously unidentified plugging mode of the HLH motif mainly come from two parts, namely, the CHP1-HC1 complex and the NHE3 cavity (Fig. 3, B and C). In this instance,  $\text{Y625}^{\text{HLH}}$  forms hydrogen bonds with  $\text{M142}^{\text{CHP1}}$  and  $\text{R482}^{\text{HC1}}$ , respectively, playing a bridging role among these three structural elements, including HLH motif, CHP1, and HC1 helix (Fig. 3B). Moreover, interactions within the HLH motif are extensive, providing certain rigidity for the plug itself.

The position of the plug tip inside the cavity is stabilized by interactions of  $\text{Y635}^{\text{HLH}}$ - $\text{D126}^{\text{TM3}}$ ,  $\text{R637}^{\text{HLH}}$ - $\text{D192}^{\text{TM5}}$ / $\text{E347}^{\text{TM10}}$ ,  $\text{H638}^{\text{HLH}}$ - $\text{E347}^{\text{TM10}}$ , and  $\text{E639}^{\text{HLH}}$ - $\text{K340}^{\text{TM10}}$  pairs. In particular, R637 disrupts the ion binding site from a 3- to 4- $\text{\AA}$  distance, thus competitively inhibiting potential ion binding or protonation. Moreover, we built an outward-facing model of the NHE3 protomer based on structural alignment with the outward-facing NHE1 (fig. S7, A to C). Relative movement and tilt were observed between the core and the dimerization domains, resulting in D221 being exposed to the solvent at the extracellular side and indicating that D221 is a key residue responsible for  $\text{Na}^+/\text{H}^+$  binding. Apparent clash would occur between this TMD model and the HLH motif loop (fig. S7C). In addition, the inhibitor binding cavity of NHE3 in the outward-facing conformation appears to be narrower and slimmer than that in outward-facing NHE1 (fig. S7, A and B), which may partly account for NHE3 being relatively insensitive to NHE1-specific inhibitors such as cariporide (34). In addition,  $\text{S636}^{\text{HLH}}$  approaches residue  $\text{E84}^{\text{TM2}}$  in NHE3, whose counterpart in NHE1, E131 ( $\text{E131}^{\text{NHE1}}$ ), was proposed as a pH sensor. It is hypothesized that, upon protonation,  $\text{E131}^{\text{NHE1}}$  contributes to transport by means of accelerating substrate cation release (11). In NHE3, the plug binding may disrupt the protonation of  $\text{E84}^{\text{TM2}}$ . Together, we speculate that binding of the plug competes with substrate binding, physically blocking the entrance of the inward-facing cavity and sterically inhibiting the inward-outward conformational transition in NHE3.

To investigate the functional role of this HLH motif in NHE3-CHP1, we truncated NHE3 from either S600 or H618 to the C terminus, and the corresponding complexes are referred to as  $\Delta 600^{\text{NHE3}}$ -CHP1 and  $\Delta 618^{\text{NHE3}}$ -CHP1, respectively. Of the two truncation constructs,  $\Delta 618^{\text{NHE3}}$ -CHP1 was expressed more robustly at the cell surface than  $\Delta 600^{\text{NHE3}}$ -CHP1 and, therefore, was selected for further study (fig. S8,

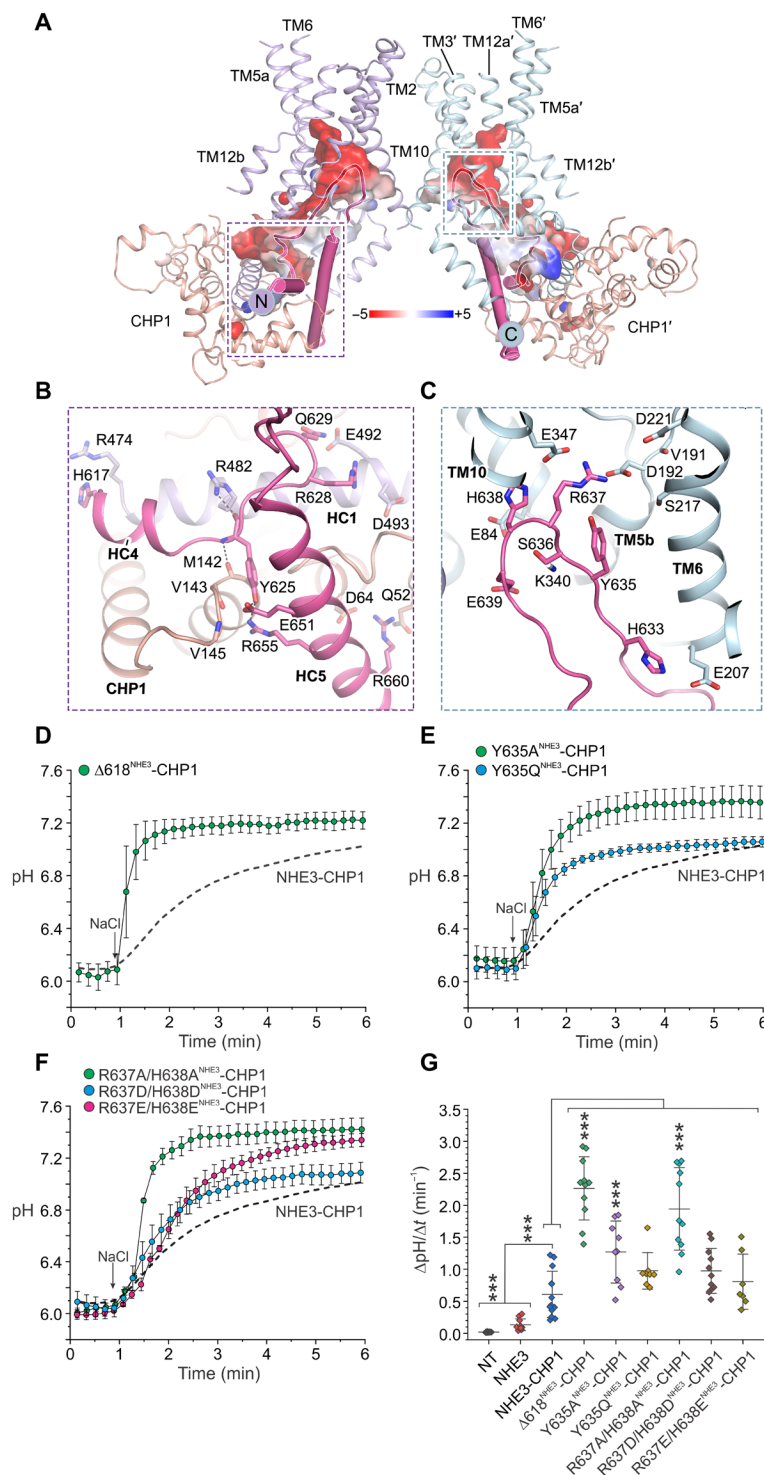


**Fig. 3. C-terminal motif blocks inward cavity as a plug. (A)** Overall view of the HLH motif. Cavity-forming helices from the TMD, i.e., TMs 2, 3, 5, 6, 10, and 12 and the electrostatic inner surface of the inward cavity in NHE3-CHP1 are displayed. Each plug is colored in magenta, and its helices are shown as cylinders. Interactions between plug helices, CHP1, and HC1 (**B**) and between the plug loop and cavity-forming helices (**C**) are shown individually. Plugs are colored in magenta, and putative interactive residues are displayed as sticks. (**D** to **F**) NHE3 activity was assessed by measuring the cytoplasmic pH following an  $\text{NH}_4^+$ -induced acidification of AP-1 cells transfected with various HLH motif mutant NHE3<sub>ChFP</sub> constructs. Recovery of pH was initiated by addition of an isotonic  $\text{Na}^+$ -rich solution (indicated by an arrow). For comparison, the pH recovery profile of wild-type NHE3-CHP1 presented in Fig. 2D is reproduced as a dashed line. Tracings are average values (means  $\pm$  SEM) from three to five cells and representative of at least two independent experiments. (**G**) NHE3 activity was defined as the initial linear rate of pH recovery as a function of time [ $\Delta\text{pH}/\Delta t$  ( $\text{min}^{-1}$ )] upon reintroduction of a  $\text{Na}^+$ -rich solution. Values represent the means  $\pm$  SD ( $n = 7$  to 13 cells from at least two independent experiments). Significance from wild-type NHE3-CHP1 was determined by one-way analysis of variance (ANOVA) with post hoc Tukey test; \*\*\* $P < 0.001$ .

B and D). Western blot and immunofluorescence colocalization assays showed that this truncation does not impair its localization in recycling endosomes nor its trafficking to the plasma membrane, and surface abundance of  $\Delta 618^{\text{NHE3}}$ -CHP1 is comparable to NHE3-CHP1 (fig. S8, A, B, and D).  $\Delta 618^{\text{NHE3}}$ -CHP1 promoted robust transport activity that was significantly greater than NHE3-CHP1 (Fig. 3, D and G). To further verify the structurally observed interactions, we mutated Y635, R637, and H638 in the HLH motif. Among them, both  $Y635A^{\text{NHE3}}$ -CHP1 and  $Y635Q^{\text{NHE3}}$ -CHP1 complexes were properly sorted to Tf-Alexa<sup>488</sup>-labeled recycling endosomes yet showed reduced surface protein abundance (fig. S8, A, C, and D) while nevertheless exhibiting increased rates of transport activity relative to NHE3-CHP1 (Fig. 3, E and G). Similar results were also obtained with the double-mutation  $R637A/H638A^{\text{NHE3}}$ , presumably by abolishing the plug binding into the cavity that elevated the intrinsic rates of ion translocation (Fig. 3, F and G). These results further support an autoinhibitory role for the HLH motif. Unexpectedly, the double mutations  $R637E/H638E^{\text{NHE3}}$  and  $R637D/H638D^{\text{NHE3}}$  did not relieve the autoinhibition as strongly as  $R637A/H638A^{\text{NHE3}}$  (Fig. 3, F and G, and fig. S8, A, C, and D). These results suggest that the charge-flipping mutations may have forced the plug loop into an alternative conformation that is still able to partially block the entrance of the cavity. For instance, the introduced acidic residues may electrostatically interact with basic residues (e.g., K340) around the entrance of the cavity (Fig. 3C).

Because the autoinhibition mediated by the plug binding is all or none in nature, this process must be fine-tuned to regulate NHE3-CHP1 activity. Possible tuning signals may come from specific binding of auxiliary proteins to the plug, phosphorylation, and other chemical modifications to prevent or destabilize the autoinhibition. By analyzing the rate of pH elevation ( $\Delta\text{pH}/\Delta t$ ) of NHE3-CHP1 and  $\Delta 618^{\text{NHE3}}$ -CHP1 (assuming the latter is fully activated; Fig. 3G), we estimate that approximately two of three of all NHE3 molecules on the plasma membrane stay autoinhibited.

On the basis of sequence homology (fig. S9), we postulated that the HLH motif in both NHE1 and NHE3 share similar structure and function. Regulation of the activity of NHE1 by an interaction between calmodulin (CaM) and a putative C-terminal regulatory domain has been reported (35). In addition, the crystal structure of CaM-HLH motif in NHE1 was reported (36), in which half the plug loop assumes helical conformation and extends HC4, comparing with that observed in our NHE3 structure. Although speculative, the following scenario may offer some clues to regulation of NHE1 activity: When not bound to CaM, NHE1 is likely stabilized at an inward-facing conformation by the HLH motif. Upon increases in  $[\text{Ca}^{2+}]_{\text{in}}$ , the  $\text{Ca}^{2+}$ -bound CaM exposes hydrophobic target-binding surfaces before exhibiting stronger affinity to the HLH motif, as illustrated by the crystal structure of the CaM-HLH motif<sup>NHE1</sup> complex, and thus promotes dissociation of the plug from the inward-facing cavity of NHE1, abolishing the autoinhibition. To support such a regulation mechanism in NHE1, phosphorylation of S648<sup>NHE1</sup> inside the plug loop by protein kinase B/Akt abrogates CaM binding and reduces NHE1 activity (37). Moreover, a previous study reported that phosphorylation of S607<sup>NHE3</sup> (S605 in rat NHE3) is essential for cyclic adenosine monophosphate (cAMP)-mediated inhibition of NHE3 (38). On the basis of the sequence alignment, these two critical phosphorylation sites are not equivalent in NHE1 and NHE3 (fig. S9), implying that a different mechanism may be involved in releasing NHE3 from the inhibited state mediated by the HLH

motif, which is supported by the fact that CaM does not regulate NHE3 (39). Previous studies suggested that the NHE3 can form a complex with  $\text{Na}^+/\text{H}^+$  exchanger regulatory factor protein, cytoskeletal protein ezrin, and PKA (cAMP-dependent protein kinase), which may relay the cAMP signals that inhibit NHE3 (40). Further studies are required to understand the structural basis underlying this mechanism.

### The binding site of PIs in NHE3

Followed by previous reports that PI derivatives enhance transport activity of the NHE3-CHP1 complex (23, 25), we found two PI-like lipid molecules bound to our complex structure (Fig. 4A and fig. S3). Each lipid molecule binds to a cytoplasmic-side peripheric groove formed by TM4 and TM11 of the core domain (Fig. 4B). In particular, positively charged R397 from the C terminus of TM11 and H500 from the N terminus of HC2 form potential salt bridge bonds with negatively charged phosphate groups of the phospholipid molecules (Fig. 4C). These observations are consistent with a previous study suggesting that PI is able to bind with and regulate anion exchanger 1 (41). In addition to interactions between the PI molecule and the N terminus of HC2 helix, the C terminus of HC2 interacts with the cytosolic termini of TM7, TM9, and their following loops (Fig. 4D). Together with a conserved amphiphilic helix N-terminal to each TM4, these PI molecules anchor the core domain to the membrane, which might affect relative movement between the dimerization domain and the core domain and, thus, regulate the activity of NHE3. Thus, we speculate that the association of PI might also be critical for integrity and stability of the core domain during the transport cycle. In agreement, both R397A and R397D single-point mutations largely abolished transport activity without greatly affecting NHE3 surface protein expression or localization to recycling endosomes (Fig. 4, E and H, and fig. S10). The R397 is highly conserved across different NHE isoforms. The equivalent residue in NHE1 is R440 (R440<sup>NHE1</sup>). The activities of R440<sup>NHE1</sup> mutants are significantly reduced (42). The R440D<sup>NHE1</sup> caused an acidic shift in the pH dependence of activity (43, 44). Together, this conserved arginine is important for the activity potentially by interacting with PI molecules or allosterically regulating the proton binding affinity.

When H500 is substituted with alanine or aspartate, the results are completely opposite to those of the R397 mutants (Fig. 4, F and H, and fig. S10). Both mutant complexes showed markedly improved transport activity. It is probable that the mutation at H500 releases HC2 from the PI binding site (Fig. 4B), destabilizes the CHP1-HC1 module, and thus interrupts the binding of the HLH motif, favoring dissociation of the plug from the autoinhibitory position (Fig. 4A). However, combining mutations at both sites resulted in intermediate effects, with double-mutant R397A/H500A or R397D/H500D causing partial impairment or almost completely abolition of transport activity, respectively (Fig. 4, G and H, and fig. S10).

Human NHE3 plays pivotal roles in renal and intestine NaCl (re)absorption and blood pressure regulation (45). Dysfunctions of NHE3 have been implicated in several disease states. While there have been recent advances in understanding some of the general structural features (i.e., membrane topology) of certain eukaryotic NHEs (i.e., NHE1 and NHE9), there is still a significant gap in our knowledge of how the cytosolic C-terminal tail of eukaryotic NHEs and membrane phosphatidylinositol lipids precisely and controllably regulate transporter activity. Here, we studied the regulation of human NHE3 by CHP1 using a multidisciplinary combination of

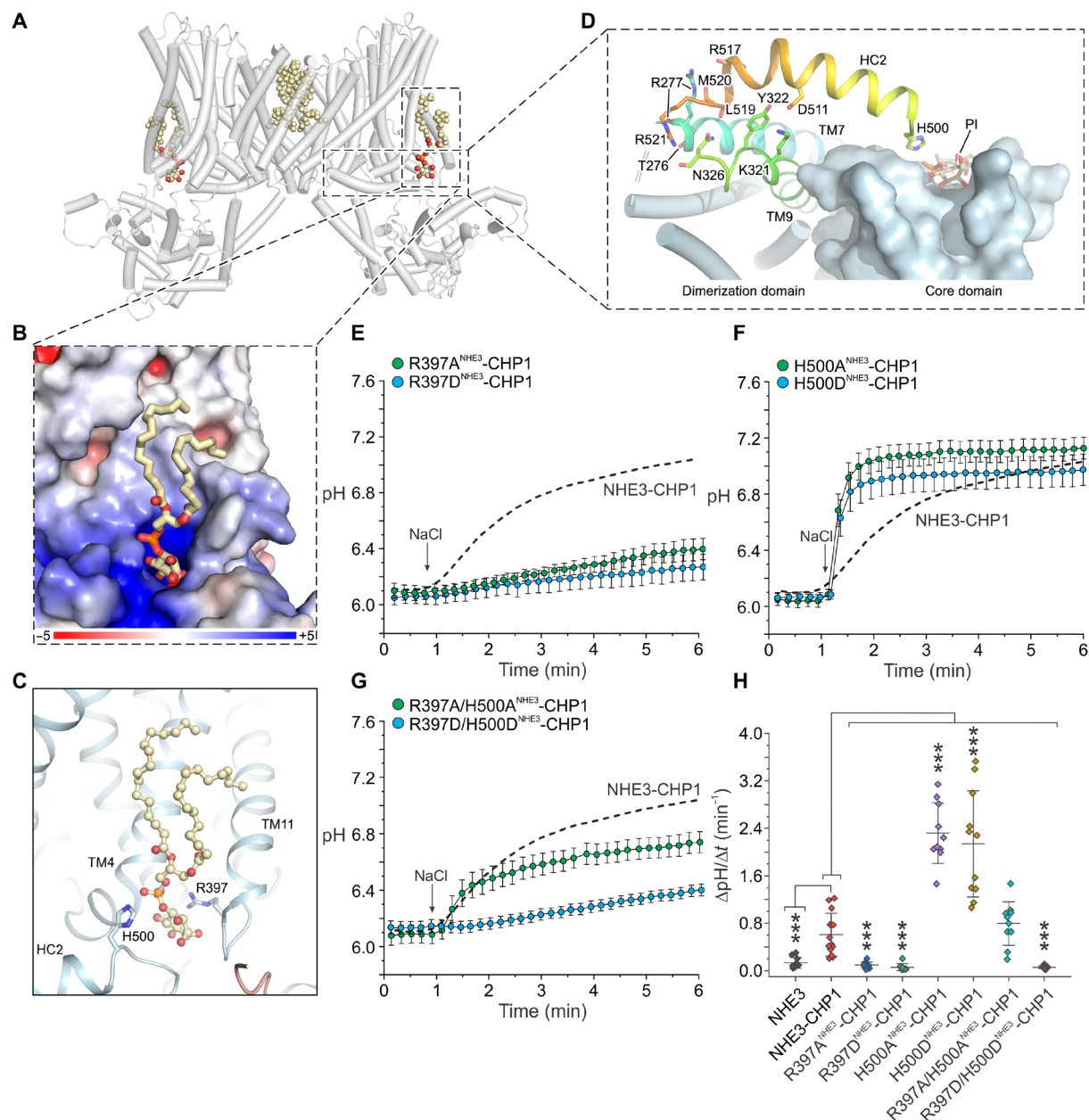


**Fig. 4. PIs bound to peripheral juxtamembrane sides.** (A) One PI molecule bound to each NHE3 subunit is displayed as spheres with colored atoms, and lipid molecules at the dimerization interface are shown in the same way, with carbon backbone in gray. (B) The electrostatic surface around PI, which is displayed as yellow stick. (C) Interactions between PI and the surrounding residues from TM4 and TM11. (D) Cytoplasmic-viewed PI and anchored HC2. The core and dimerization domain of NHE3 protomer are displayed as a blue solid surface and cylindrical cartoon, while HC2, TM7, and TM9 are displayed as a rainbow cartoon. Residues involving in HC2 stabilization together with PI are displayed as sticks and indicated. (E to G) NHE3 activity was assessed by measuring cytoplasmic pH following an  $\text{NH}_4^+$ -induced acidification of AP-1 cells transfected with the various PI-mutant NHE3 constructs. Recovery of pH was initiated by addition of an isotonic  $\text{Na}^+$ -rich solution (indicated by an arrow). For comparison, the pH recovery profile of wild-type NHE3-CHP1 presented in Fig. 2D is reproduced as a dashed line. Tracings are average values (means  $\pm$  SEM) from three to six cells and representative of two independent experiments. (H) NHE3 activity was defined as the initial linear rate of pH recovery as a function of time [ $\Delta\text{pH}/\Delta t$  (min<sup>-1</sup>)] upon reintroduction of a  $\text{Na}^+$ -rich solution. Values represent the means  $\pm$  SD ( $n = 9$  to 11 cells from two independent experiments). Significance from wild-type NHE3-CHP1 was determined by one-way ANOVA with post hoc Tukey test; \*\*\* $P < 0.001$ .

biochemical, imaging, cell-based transport assays, and structural biological approaches. We found that CHP1 not only increases the surface expression of NHE3 but also significantly boosts NHE3 transport activity. Subsequently, we carried out single-particle cryo-EM studies and determined the NHE3-CHP1 complex at a 3.2-Å resolution.

We observed the insertion of a segment of the C-terminal tail into an inward-facing cavity of NHE3, indicating that this complex is stabilized in an autoinhibited state. Consequently, the CHP1 adopts a different conformation from that of the recently reported NHE1-CHP1 complex. Moreover, we detected the presence of two phosphatidylinositol



molecules that bound to peripheral juxtamembrane sides of the complex and, by site-directed mutagenesis, was found to be fundamentally important for fine-tuning the activity of NHE3. These findings may also serve as a structural and functional paradigm for other eukaryotic NHE transporters.

## METHODS

### Expression and purification of the human NHE3-CHP1 complex

The genes of the human NHE3 (UniProtKB accession: P48764) and human CHP1 (UniProtKB accession: Q99653) were amplified from a human cDNA library. The NHE3 gene and CHP1 gene were subcloned into a modified pEG BacMam vector. A superfolder green fluorescent protein (sfGFP) and twin-strep tag were introduced at the C terminus of NHE3. The NHE3 and CHP1 genes were coexpressed in human embryonic kidney (HEK) 293F cells using the Bac-to-Bac baculovirus expression system (Invitrogen, USA). P1 and P2 viruses of NHE3 and CHP1 were obtained from sf9 insect cells, respectively. HEK293F cells were infected by P2 viruses of both genes at the same time, supplemented with 1% (v/v) fetal bovine serum. The cells were cultured at 37°C in suspension and 5% CO<sub>2</sub> in a shaking incubator. Sodium butyrate (10 mM) was added after 12 hours. Subsequently, the cells were harvested after another 48 hours and were stored at –80°C immediately after being frozen in liquid nitrogen.

The cells expressing NHE3-CHP1 complex were resuspended in purification buffer A [20 mM Hepes (pH 7.5), 150 mM NaCl, 5 mM  $\beta$ -mercaptoethanol ( $\beta$ -ME), and protease inhibitor cocktail (Roche, Swiss)]. The membranes were then broken using a Dounce homogenizer and were collected by centrifugation at 100,000g for 1 hour and solubilized in solubilization buffer B [20 mM Hepes (pH 7.5), 150 mM NaCl, 5 mM  $\beta$ -ME, 2  $\mu$ M CaCl<sub>2</sub>, 1% (w/v) *n*-dodecyl  $\beta$ -D-maltoside (Anatrace), and 0.2% (w/v) cholesteryl hemisuccinate (Anatrace)] at 4°C for 2 hours with rotation. Subsequently, the insoluble cell debris was removed by centrifugation at 100,000g for 1 hour. The supernatant was passed through Streptactin Beads (Smart-Lifesciences, China) pre-equilibrated with wash buffer C [20 mM Hepes (pH 7.5), 150 mM NaCl, 5 mM  $\beta$ -ME, 2  $\mu$ M CaCl<sub>2</sub>, and 0.01% (w/v) glycodiosgenin (GDN)]. The beads were washed with 10 column volumes of wash buffer supplemented with 5 mM ATP and 5 mM MgCl<sub>2</sub>. The NHE3-CHP1 complex was eluted with the wash buffer supplemented with 5 mM desthiobiotin. The eluted protein was subsequently concentrated in the 100-kDa molecular weight cutoff spin concentrators (Merck Millipore, Germany) and further purified by gel filtration (Superose 6 Increase 10/300 GL, GE Healthcare, USA) pre-equilibrated in the wash buffer. The peak fractions between 11.5 and 13.5 ml were pooled and concentrated to about 2 mg/ml for nanodisc reconstitution.

### Nanodisc reconstitution

The NHE3-CHP1 complexes and 1-palmitoyl-2-oleoyl-sn-glycero-3-phosphocholine (POPC) lipid were reconstituted into membrane scaffold protein 1D1 (MSP1D1) nanodiscs at a molar ratio (dimer NHE3-CHP1:MSP1D1:POPC) of 1:5:50. First, the POPC lipid (25 mg/ml) was suspended in the purification buffer supplemented with 2% (w/v) GDN. The NHE3-CHP1 complex protein and MSP1D1 were then added to the lipids in proportion and inverted at 4°C for 1 hour with rotation. Subsequently, the mixture was added into Bio-Beads SM2

(400 mg/ml) to remove detergent and incubated at 4°C for 2 hours with rotation and repeated three times. The mixture was incubated overnight after the final addition of Bio-Beads. Then, the Bio-Beads were removed and the mixture was added into PreScission Protease (PPase) to digest the sfGFP-StrepII tag of NHE3. For further purification, the protein complex was concentrated and subjected to a Superose 6 Increase 10/300 GL gel filtration column (GE Healthcare, USA) pre-equilibrated in the solubilization buffer B without detergent. The peak fractions were pooled and concentrated to about 3.0 mg/ml for cryo-EM sample preparation.

### Cryo-EM sample preparation and data acquisition

A droplet of 2.5  $\mu$ l of the purified NHE3-CHP1 protein sample (3 mg/ml) was applied on glow-discharged holey carbon grids (Au R1.2/1.3 300 mesh, QUANTIFOIL). The grids were then automatically blotted for 3.5 s at 4°C under 100% humidity using a Vitrobot Mark IV (Thermo Fisher Scientific, USA) and vitrified in liquid ethane. The grids were then transferred to a Titan Krios G2 operating at 300 kV, and cryo-EM data were collected by a K2 Summit direct electron detector with a GIF quantum LS energy filter. The slit width of energy filter was set to 20 eV. Movie stacks were collected using SerialEM 3.8 (46) at the nominal magnification of  $\times 130,000$ , generating a superresolution pixel size of 1.04 Å on images. The dose rate and exposure time were set to  $\sim 9.2$  Å/pixel/s and 7.04 s, respectively, yielding a total dose of 60 e<sup>–</sup>/Å<sup>2</sup> on the image. The defocus range was set to the range between –1.2 and –2.2  $\mu$ m.

### Data processing

A total of 2321 movie stacks were collected. Motion correction was performed using MotionCor2 (47) using 5  $\times$  5 patches. Parameters of contrast transfer function (CTF) were estimated using GCTF (48). Particle picking using Gautomatch yielded an initial dataset of 1419k particles, followed by rounds of two-dimensional (2D) and 3D classifications in RELION-3.0 (49) to clean false-positive particles. The first round of 3D classification generated eight classes. The most populated class 8 (31%) that was selected for further processing displayed nanodisc densities, large soluble domains, and TMD, which features the conventional NHE-like shape. Subsequent 3D autorefinement generated a 3.9-Å map. To improve the map quality, another round of 3D classification was conducted, resulting to three classes. Class 1 (17%) displayed high-resolution structural features including continuous TM helices, side chains, and well-resolved CHP1 subunits and was thus submitted for 3D autorefinement, which generated a 3.7-Å map. Bayesian polishing and CTF refinement were then conducted on the particle dataset, and the final map was reported at 3.2 Å according to gold-standard Fourier shell correlation (50) criterion.

### Model building and structural analysis

The model of the inward-facing NHE1-CHP1 complex [Protein Data Bank (PDB) ID: 7DSV] was selected as the starting model because of sequence similarity and homology. Sequence alignment between NHE3 and NHE1 was conducted, and residues in the NHE3 model were manually mutated and adjusted according to the alignment result. The high-resolution features of both NHE3 and CHP1 in the map enabled us to unambiguously assign the side chain of most residues. The manually built model was refined against the corresponding EM map using the real-space refinement tool in the PHENIX (51) software package with twofold symmetry. The validation of the model was performed using the comprehensive validation (cryo-EM) in PHENIX.



The outward-facing NHE3 protomer model was constructed on the basis of the outward-facing NHE1-CHP1 complex (PDB ID: 7DSX) in Chimera (52). Specifically, the inward-facing hNHE3 protomer was segmented into dimerization domain and core domain, which subsequently were overlaid onto the outward-facing hNHE1 complex independently. The resulting PDBs were combined in COOT, resulting in an outward-facing hNHE3. Solvent accessible areas in the text were calculated using command ACCESS in EDPDB (53). A van der Waals radius of 1.4 Å was assigned while calculating. The hydrophobic surface of CHP1 was calculated by command “mlp” in ChimeraX, which is based on pyMLP (Molecular Lipophilicity Potential evaluator) (54, 55). All structure figures are prepared using PyMOL and ChimeraX (56).

### Cell culture

Chinese hamster ovary AP-1 cells are a mutagenized cell line devoid of plasma membrane NHE expression (26). AP-1 cells were cultured in  $\alpha$ -minimum essential medium ( $\alpha$ -MEM) supplemented with 10% fetal bovine serum, penicillin (100 U/ml), streptomycin (100  $\mu$ g/ml), and 25 mM NaHCO<sub>3</sub> (pH 7.4).

### Western blotting

For Western blot analyses, AP-1 cells were grown in 35-mm dishes and transiently transfected with 1.5  $\mu$ g of plasmid DNA encoding wild-type human NHE3 tagged at its C terminus with mCherry (simply NHE3) alone or wild-type and mutant NHE3 and CHP1 constructs using Lipofectamine 2000 (Invitrogen) according to the manufacturer's recommended procedure. Cell lysates were prepared following 24 hours after transfection by washing cells twice on ice with ice-cold phosphate-buffered saline (PBS), followed by scraping in 0.5 ml of lysis buffer [0.5% NP40/0.25% sodium deoxycholate/PBS supplemented with protease inhibitor cocktail (Roche Diagnostics)]. Lysates were incubated for 30 min on a rocker at 4°C and then centrifuged for 20 min at 4°C to pellet the nuclei and cellular debris. Forty micrograms of protein from the resulting supernatants was eluted in SDS sample buffer [50 mM Tris-HCl (pH 6.8), 1% SDS, 50 mM dithiothreitol, 10% glycerol, and 1% bromophenol blue], subjected to 8 or 12% SDS-polyacrylamide gel electrophoresis (SDS-PAGE), and then transferred to polyvinylidene fluoride membranes (Millipore, Nepean, ON, Canada) for immunoblotting. The membranes were blocked with 5% nonfat skim milk for 1 hour and then incubated with the following specified primary mouse monoclonal antibodies: anti-ChFP (1:500; Abcam, ab125096), anti-NHE3 (1:5000; Millipore-Sigma, clone 3H3, catalog no. MABN1813), anti-CHP1 (1:1000; OTI4B9; Thermo Fisher Scientific/Invitrogen, catalog no. MA5-27271), anti-ATP1A1 (1:2000; Thermo Fisher Scientific/Invitrogen, catalog no. MA3-929), and anti- $\beta$ -tubulin (1:10,000; Millipore-Sigma, catalog no. T0198) in PBS containing 0.1% Tween 20, followed by extensive washes and incubation with goat anti-mouse horseradish peroxidase-conjugated secondary antibodies (ChFP, 1:3000; NHE3, 1:4000; CHP1, 1:3000; ATP1A1, 1:3000; and  $\beta$ -tubulin, 1:10,000) for 1 hour at room temperature. Immunoreactive bands were detected using Western Lightning Plus-ECL blotting detection reagents (PerkinElmer Inc., Waltham, MA).

### Cell surface biotinylation

AP-1 cells expressing wild-type or mutant NHE3 constructs in the absence or presence of CHP1 were cultured in 10-cm dishes to subconfluence, placed on ice, and washed three times with ice-cold PBS

containing 1 mM MgCl<sub>2</sub> and 0.1 mM CaCl<sub>2</sub> (pH 8.0) (PBS-CM). Next, cells were incubated at 4°C for 30 min with the membrane-impermeable reagent *N*-hydroxysulfosuccinimide-SS-biotin (0.5 mg/ml; Thermo Fisher Scientific). Cells were washed and incubated twice in quenching buffer (50 mM glycine in PBS-CM) for 7 min each on ice to remove the unreacted biotin. After two more washes in PBS-CM, the cells were lysed for 30 min on ice and then centrifuged at 16,000g for 20 min at 4°C to remove insoluble cellular debris. A fraction of the resulting supernatant containing 1 mg of total protein was removed, and this represents the total fraction. The remaining supernatant was incubated with 100  $\mu$ l of 50% NeutrAvidin Agarose Resin slurry (Thermo Fisher Scientific) in lysis buffer overnight at 4°C to extract biotinylated membrane proteins. The proteins were then resolved by SDS-PAGE and analyzed by Western blotting.

### Immunofluorescence confocal microscopy

AP-1 cells were cultured on fibronectin-coated 18-mm glass coverslips, transfected with the NHE3<sub>ChFP</sub> constructs for 24 hours, incubated with Alexa Fluor 488-conjugated transferrin (Tf-Alexa<sup>488</sup>) for 45 min in serum-free  $\alpha$ -MEM, washed, and fixed with 4% paraformaldehyde for 20 min at room temperature. Nuclei were labeled with DNA dye 4',6-diamidino-2-phenylindole (1:5000) for 15 min at room temperature. Coverslips were mounted, and cells were examined by laser scanning confocal microscopy using the ZEN software of a Zeiss LSM 780 microscope equipped with a photomultiplier tube detector, with images acquired using a 63 $\times$ /1.4 NA (numerical aperture) oil immersion objective lens.

### Measurements of cytoplasmic pH

AP-1 cells were grown in 35-mm dishes and transiently transfected with 2  $\mu$ g of mCherry (ChFP), wild-type NHE3<sub>ChFP</sub>, or the indicated mutants using Lipofectamine 2000 according to the manufacturer's instructions. Five hours after transfection, the cells were split and seeded onto fibronectin-coated [2  $\mu$ g/ml in PBS (pH 7.4) overnight at 4°C] FluoroDishes and grown overnight.

To measure the cytoplasmic pH, the cells were washed in a Na<sup>+</sup>-rich solution [140 mM NaCl, 5 mM KCl, 1 mM CaCl<sub>2</sub>, 1 mM MgCl<sub>2</sub>, 10 mM glucose, and 10 mM Hepes-Na<sup>+</sup> (pH 7.4)] three times and incubated with the pH-sensitive dye BCECF-AM [2',7'-bis-(2-carboxyethyl)-5-(and 6)-carboxyfluorescein-acetoxymethyl ester] (5  $\mu$ M) diluted in a Na<sup>+</sup>-rich solution for 30 min at 37°C. Cells were subsequently washed four times in a Na<sup>+</sup>-rich solution and subjected to ratiometric imaging using an inverted fluorescence microscope (IX81, Olympus, Center Valley, PA) and imaging system (Photon Technology International, Edison, NJ). Experiments were carried out at 37°C using a thermostatically controlled platform (FC-5, Live Cell Instr., Seoul, Korea). Flow rate was maintained at 1 ml/min using a four-channel peristaltic pump (205S, Watson Marlow, Wilmington, MA). Intracellular BCECF was excited alternately at 440 and 490 nm every 10 s. Transfected cells were identified by detecting mCherry fluorescence. The fluorescence intensities were measured using the EasyRatioPro software (Horiba Sci., Mississauga, ON). Fluorescence ratios (F490/F440) were recorded and displayed continuously. The F490/F440 ratios were converted to pH using the K<sup>+</sup>-nigericin clamp method (57). Briefly, AP-1 cells were loaded with BCECF-AM, and in situ calibration was performed by clamping the cytoplasmic pH between 6 and 8.5 in a K<sup>+</sup>-rich solution (135 mM KCl, 10 mM NaCl, 20 mM Hepes, 1 mM MgCl<sub>2</sub>, and

0.1 mM CaCl<sub>2</sub>) containing 10 μM nigericin and recording the fluorescence ratios.

To measure NHE3 activity, AP-1 transfectants were subjected to an NH<sub>4</sub>Cl-induced acid load (58, 59) and then the initial rates of Na<sup>+</sup>-dependent pH recovery were measured as a function of time [ $\Delta\text{pH}/\Delta t$  (min<sup>-1</sup>)]. The rates were calculated on the basis of the initial linear phase of the pH recovery. Briefly, baseline fluorescence ratios were recorded for 5 min in a Na<sup>+</sup>-rich solution, followed by an acute acid load induced by incubating the cells for 5 min in isotonic NH<sub>4</sub>Cl solution [50 mM NH<sub>4</sub>Cl, 70 mM choline chloride, 5 mM KCl, 1 mM MgCl<sub>2</sub>, 2 mM CaCl<sub>2</sub>, 5 mM glucose, and 20 mM Hepes-tris (pH 7.4)], followed by 10 min in an isotonic Na<sup>+</sup>-free solution [125 mM choline chloride, 1 mM MgCl<sub>2</sub>, 2 mM CaCl<sub>2</sub>, 5 mM glucose, and 20 mM Hepes-tris (pH 7.4)]. pH recovery was measured for 15 min upon reintroduction of a Na<sup>+</sup>-rich solution. Graphics were performed using the Origin 2020 software.

## Statistical analyses

Statistical analyses were performed using the Origin 2020 software. The data are presented as the means ± SD unless stated otherwise. Means of multiple samples were compared using a one-way analysis of variance (ANOVA) followed by post hoc Tukey test as indicated. To satisfy conditions for ANOVA, the homogeneity of group variances was evaluated using the Levene and Brown-Forsythe tests. For datasets where the population variances were significantly different (0.05 level), the data were subjected to a logarithmic transformation to minimize within group variances before the ANOVA. A minimum *P* value of <0.05 was considered significant.

## SUPPLEMENTARY MATERIALS

Supplementary material for this article is available at <https://science.org/doi/10.1126/sciadv.abn3925>

[View/request a protocol for this paper from Bio-protocol.](#)

## REFERENCES AND NOTES

- N. Lane, W. F. Martin, The origin of membrane bioenergetics. *Cell* **151**, 1406–1416 (2012).
- S. F. Pedersen, L. Counillon, The SLC9A-C mammalian Na<sup>+</sup>/H<sup>+</sup> exchanger family: Molecules, mechanisms, and physiology. *Physiological Rev.* **99**, 2015–2113 (2019).
- J. Orlowski, S. Grinstein, Na<sup>+</sup>/H<sup>+</sup> exchangers. *Compr. Physiol.* **1**, 2083–2100 (2011).
- P. J. Schultheis, L. L. Clarke, P. Meneton, M. L. Miller, M. Soleimani, L. R. Gawanis, T. M. Riddle, J. J. Duffy, T. Doetschman, T. Wang, G. Giebisch, P. S. Aronson, J. N. Lorenz, G. E. Shull, Renal and intestinal absorptive defects in mice lacking the NHE3 Na<sup>+</sup>/H<sup>+</sup> exchanger. *Nat. Genet.* **19**, 282–285 (1998).
- M. W. Hess, I. M. Krainer, P. A. Filipek, B. Witting, K. Gutleben, I. Viator, H. Zoller, D. Aldrian, E. Sturm, J. R. Goldenring, A. R. Janacke, T. Müller, L. A. Huber, G. F. Vogel, Advanced microscopy for liver and gut ultrastructural pathology in patients with MVID and PFIC caused by MYO5B mutations. *J. Clin. Med.* **10**, 1901 (2021).
- Y. Chen, S. Wu, L. Qi, W. Dai, Y. Tian, J. Kong, Altered absorptive function in the gall bladder during cholesterol gallstone formation is associated with abnormal NHE<sub>3</sub> complex formation. *J. Physiol. Biochem.* **76**, 427–435 (2020).
- Q. Tan, G. Stefano, X. Tan, X. Renjie, D. Römermann, S. R. Talbot, U. E. Seidler, Inhibition of Na<sup>+</sup>/H<sup>+</sup> exchanger isoform 3 improves gut fluidity and alkalinity in cystic fibrosis transmembrane conductance regulator-deficient and F508del mutant mice. *Br. J. Pharmacol.* **178**, 1018–1036 (2021).
- S. Yeruva, K. Farkas, J. Hubricht, K. Röde, B. Riederer, O. Bachmann, A. Cinar, Z. Rakonczay, T. Molnár, F. Nagy, J. Wedemeyer, M. Manns, D. Raddatz, M. W. Musch, E. B. Chang, P. Hegyi, U. Seidler, Preserved Na(+)/H(+) exchanger isoform 3 expression and localization, but decreased NHE<sub>3</sub> function indicate regulatory sodium transport defect in ulcerative colitis. *Inflamm. Bowel Dis.* **16**, 1149–1161 (2010).
- S. Priyamvada, R. Gomes, R. K. Gill, S. Saksena, W. A. Alrefai, P. K. Dudeja, Mechanisms underlying dysregulation of electrolyte absorption in inflammatory bowel disease-associated diarrhea. *Inflamm. Bowel Dis.* **21**, 2926–2935 (2015).
- A. R. Janacke, P. Heinz-Erian, J. Yin, B. S. Petersen, A. Franke, S. Lechner, I. Fuchs, S. Melancon, H. H. Uhlig, S. Travis, E. Marinier, V. Perisic, N. Ristic, P. Gerner, I. W. Booth, S. Wedenoja, N. Baumgartner, J. Vodopivec, M. C. Frechette-Duval, J. de Lafollie, R. Persad, N. Warner, C. M. Tse, K. Sud, N. C. Zachos, R. Sarker, X. Zhu, A. M. Muise, K. P. Zimmer, H. Witt, H. Zoller, M. Donowitz, T. Müller, Reduced sodium/proton exchanger NHE<sub>3</sub> activity causes congenital sodium diarrhea. *Hum. Mol. Genet.* **24**, 6614–6623 (2015).
- Y. Dong, Y. Gao, A. Ilie, D. S. Kim, A. Boucher, B. Li, X. C. Zhang, J. Orlowski, Y. Zhao, Structure and mechanism of the human NHE1-CHP1 complex. *Nat. Commun.* **12**, 3474 (2021).
- I. Winklemann, R. Matsuoka, P. F. Meier, D. Shutin, C. Zhang, L. Orellana, R. Sexton, M. Landreh, C. V. Robinson, O. Beckstein, D. Drew, Structure and elevator mechanism of the mammalian sodium/proton exchanger NHE<sub>9</sub>. *EMBO J.* **39**, 4541–4559 (2020).
- C. Hunte, E. Screpanti, M. Venturi, A. Rimón, E. Padan, H. Michel, Structure of a Na<sup>+</sup>/H<sup>+</sup> antiporter and insights into mechanism of action and regulation by pH. *Nature* **435**, 1197–1202 (2005).
- C. Paulino, D. Wöhlert, E. Kapotova, Ö. Yildiz, W. Kühlbrandt, Structure and transport mechanism of the sodium/proton antiporter MjNhaP1. *eLife* **3**, e03583 (2014).
- D. Wöhlert, W. Kühlbrandt, O. Yildiz, Structure and substrate ion binding in the sodium/proton antiporter PaNhaP. *eLife* **3**, e03579 (2014).
- C. Lee, H. J. Kang, C. von Ballmoos, S. Newstead, P. Uzdavins, D. L. Dotson, S. Iwata, O. Beckstein, A. D. Cameron, D. Drew, A two-domain elevator mechanism for sodium/proton antiporter. *Nature* **501**, 573–577 (2013).
- M. Coincon, P. Uzdavins, E. Nji, D. L. Dotson, I. Winklemann, S. Abdul-Hussein, A. D. Cameron, O. Beckstein, D. Drew, Crystal structures reveal the molecular basis of ion translocation in sodium/proton antiporters. *Nat. Struct. Mol. Biol.* **23**, 248–255 (2016).
- T. Pang, X. Su, S. Wakabayashi, M. Shigekawa, Calcineurin homologous protein as an essential cofactor for Na<sup>+</sup>/H<sup>+</sup> exchangers. *J. Biol. Chem.* **276**, 17367–17372 (2001).
- B. Bertrand, S. Wakabayashi, T. Ikeda, J. Pouyssegur, M. Shigekawa, The Na<sup>+</sup>/H<sup>+</sup> exchanger isoform 1 (NHE1) is a novel member of the calmodulin-binding proteins. Identification and characterization of calmodulin-binding sites. *J. Biol. Chem.* **269**, 13703–13709 (1994).
- S. Wakabayashi, T. Ikeda, T. Iwamoto, J. Pouyssegur, M. Shigekawa, Calmodulin-binding autoinhibitory domain controls "pH-sensing" in the Na<sup>+</sup>/H<sup>+</sup> exchanger NHE<sub>1</sub> through sequence-specific interaction. *Biochemistry* **36**, 12854–12861 (1997).
- C. H. C. Yun, S. Oh, M. Zizak, D. Stepić, S. Tsao, C.-M. Tse, E. J. Weinman, M. Donowitz, cAMP-mediated inhibition of the epithelial brush border Na<sup>+</sup>/H<sup>+</sup> exchanger, NHE<sub>3</sub>, requires an associated regulatory protein. *Proc. Natl. Acad. Sci. U.S.A.* **94**, 3010–3015 (1997).
- O. Aharonovitz, H. C. Zaun, T. Balla, J. D. York, J. Orlowski, S. Grinstein, Intracellular pH regulation by Na<sup>+</sup>/H<sup>+</sup> exchange requires phosphatidylinositol 4,5-bisphosphate. *J. Cell Biol.* **150**, 213–224 (2000).
- S. Mohan, C. M. Tse, S. B. Gabelli, R. Sarker, B. Cha, K. Fahie, M. Nadella, N. C. Zachos, B. Tu-Sekine, D. Raben, L. M. Amzel, M. Donowitz, NHE3 activity is dependent on direct phosphoinositide binding at the N terminus of its intracellular cytosolic region. *J. Biol. Chem.* **285**, 34566–34578 (2010).
- B. G. Abu Jawdeh, S. Khan, I. Deschênes, M. Hoshi, M. Goel, J. T. Lock, K. Shinlapawattayatorn, G. Babcock, S. Lakhe-Reddy, G. DeCaro, S. P. Yadav, M. L. Mohan, S. V. Naga Prasad, W. P. Schilling, E. Ficker, J. R. Schelling, Phosphoinositide binding differentially regulates NHE1 Na<sup>+</sup>/H<sup>+</sup> exchanger-dependent proximal tubule cell survival. *J. Biol. Chem.* **286**, 42435–42445 (2011).
- V. Babich, F. Di Sole, The Na<sup>+</sup>/H<sup>+</sup> exchanger-3 (NHE<sub>3</sub>) activity requires ezrin binding to phosphoinositide and its phosphorylation. *PLOS ONE* **10**, e0129306 (2015).
- D. Rotin, S. Grinstein, Impaired cell volume regulation in Na(+)-H+ exchange-deficient mutants. *Am. J. Physiol.* **257**, C1158–C1165 (1989).
- D. Biemesderfer, P. A. Rutherford, T. Nagy, J. H. Pizzonia, A. K. Abu-Alfa, P. S. Aronson, Monoclonal antibodies for high-resolution localization of NHE3 in adult and neonatal rat kidney. *Am. J. Physiol.* **273**, F289–F299 (1997).
- R. T. Alexander, W. Furuya, K. Szász, J. Orlowski, S. Grinstein, Rho GTPases dictate the mobility of the Na/H exchanger NHE<sub>3</sub> in epithelia: Role in apical retention and targeting. *Proc. Natl. Acad. Sci. U.S.A.* **102**, 12253–12258 (2005).
- S. D'Souza, A. Garcia-Cabado, F. Yu, K. Teter, G. Lukacs, K. Skorecki, H. P. Moore, J. Orlowski, S. Grinstein, The epithelial sodium-hydrogen antiporter Na<sup>+</sup>/H<sup>+</sup> exchanger 3 accumulates and is functional in recycling endosomes. *J. Biol. Chem.* **273**, 2035–2043 (1998).
- C. R. Hopkins, Intracellular routing of transferrin and transferrin receptors in epidermoid carcinoma A431 cells. *Cell* **35**, 321–330 (1983).
- M. Zizak, M. E. Cavet, D. Bayle, C. M. Tse, S. Hallen, G. Sachs, M. Donowitz, Na<sup>+</sup>/H<sup>+</sup> exchanger NHE<sub>3</sub> has 11 membrane spanning domains and a cleaved signal peptide: Topology analysis using in vitro transcription/translation. *Biochemistry* **39**, 8102–8112 (2000).
- C. Cecchetti, E. Pyle, B. Byrne, Transporter oligomerisation: Roles in structure and function. *Biochem. Soc. Trans.* **47**, 433–440 (2019).
- M. Mishima, S. Wakabayashi, C. Kojima, Solution structure of the cytoplasmic region of Na<sup>+</sup>/H<sup>+</sup> exchanger 1 complexed with essential cofactor calcineurin B homologous protein 1. *J. Biol. Chem.* **282**, 2741–2751 (2007).

34. J. Orlowski, Heterologous expression and functional properties of amiloride high affinity (NHE<sub>1</sub>-) and low affinity (NHE<sub>3</sub>-) isoforms of the rat Na/H exchanger. *J. Biol. Chem.* **268**, 16369–16377 (1993).
35. S. Wakabayashi, T. Hisamitsu, T. Y. Nakamura, Regulation of the cardiac Na<sup>+</sup>/H<sup>+</sup> exchanger in health and disease. *J. Mol. Cell. Cardiol.* **61**, 68–76 (2013).
36. S. Köster, T. Pavkov-Keller, W. Kühlbrandt, Ö. Yildiz, Structure of human Na<sup>+</sup>/H<sup>+</sup> exchanger NHE1 regulatory region in complex with calmodulin and Ca<sup>2+</sup>. *J. Biol. Chem.* **286**, 40954–40961 (2011).
37. A. K. Snabaitis, F. Cuello, M. Avkiran, Protein kinase B/Akt phosphorylates and inhibits the cardiac Na<sup>+</sup>/H<sup>+</sup> exchanger NHE1. *Circ. Res.* **103**, 881–890 (2008).
38. K. Kurashima, F. H. Yu, A. G. Cabado, E. Z. Szabó, S. Grinstein, J. Orlowski, Identification of sites required for down-regulation of Na<sup>+</sup>/H<sup>+</sup> exchanger NHE<sub>3</sub> activity by cAMP-dependent protein kinase. phosphorylation-dependent and -independent mechanisms. *J. Biol. Chem.* **272**, 28672–28679 (1997).
39. S. Wakabayashi, T. Ikeda, J. Noël, B. Schmitt, J. Orlowski, J. Pouyssegur, M. Shigekawa, Cytoplasmic domain of the ubiquitous Na<sup>+</sup>/H<sup>+</sup> exchanger NHE<sub>1</sub> can confer Ca<sup>2+</sup> responsiveness to the apical isoform NHE<sub>3</sub>. *J. Biol. Chem.* **270**, 26460–26465 (1995).
40. C. H. Yun, G. Lamprecht, D. V. Forster, A. Sidor, NHE<sub>3</sub> kinase A regulatory protein E3KARP binds the epithelial brush border Na<sup>+</sup>/H<sup>+</sup> exchanger NHE<sub>3</sub> and the cytoskeletal protein ezrin. *J. Biol. Chem.* **273**, 25856–25863 (1998).
41. D. De Vecchis, R. A. F. Reithmeier, A. C. Kalli, Molecular simulations of intact anion exchanger 1 reveal specific domain and lipid interactions. *Biophys. J.* **117**, 1364–1379 (2019).
42. K. Y. Wong, R. McKay, Y. Liu, K. Towle, Y. Elloumi, X. Li, S. Quan, D. Dutta, B. D. Sykes, L. Fliegel, Diverse residues of intracellular loop 5 of the Na<sup>+</sup>/H<sup>+</sup> exchanger modulate proton sensing, expression, activity and targeting. *Biochim. Biophys. Acta Biomembr.* **1861**, 191–200 (2019).
43. S. Wakabayashi, T. Hisamitsu, T. Pang, M. Shigekawa, Kinetic dissection of two distinct proton binding sites in Na<sup>+</sup>/H<sup>+</sup> exchangers by measurement of reverse mode reaction. *J. Biol. Chem.* **278**, 43580–43585 (2003).
44. S. Wakabayashi, T. Hisamitsu, T. Pang, M. Shigekawa, Mutations of Arg440 and Gly455/ Gly456 oppositely change pH sensing of Na<sup>+</sup>/H<sup>+</sup> exchanger 1. *J. Biol. Chem.* **278**, 11828–11835 (2003).
45. B. Linz, A. Saljic, M. Hohl, M. Gawalko, T. Jespersen, P. Sanders, M. Böhm, D. Linz, Inhibition of sodium-proton-exchanger subtype 3-mediated sodium absorption in the gut: A new antihypertensive concept. *Int. J. Cardiol. Heart Vasc.* **29**, 100591 (2020).
46. D. N. Mastronarde, Automated electron microscope tomography using robust prediction of specimen movements. *J. Struct. Biol.* **152**, 36–51 (2005).
47. S. Q. Zheng, E. Palovcak, J. P. Armache, K. A. Verba, Y. Cheng, D. A. Agard, MotionCor2: Anisotropic correction of beam-induced motion for improved cryo-electron microscopy. *Nat. Methods* **14**, 331–332 (2017).
48. K. Zhang, Gctf: Real-time CTF determination and correction. *J. Struct. Biol.* **193**, 1–12 (2016).
49. J. Zivanov, T. Nakane, B. O. Forsberg, D. Kimanius, W. J. H. Hagen, E. Lindahl, S. H. W. Scheres, New tools for automated high-resolution cryo-EM structure determination in RELION-3. *eLife* **7**, e42166 (2018).
50. S. H. W. Scheres, S. Chen, Prevention of overfitting in cryo-EM structure determination. *Nat. Methods* **9**, 853–854 (2012).
51. P. D. Adams, P. V. Afonine, G. Bunkóczi, V. B. Chen, I. W. Davis, N. Echols, J. J. Headd, L.-W. Hung, G. J. Kapral, R. W. G. Kunstleve, A. J. M. Coy, N. W. Moriarty, R. Oeffner, R. J. Read, D. C. Richardson, J. S. Richardson, T. C. Terwilliger, P. H. Zwart, PHENIX: A comprehensive Python-based system for macromolecular structure solution. *Acta Crystallogr. D Biol. Crystallogr.* **66**, 213–221 (2010).
52. E. F. Pettersen, T. D. Goddard, C. C. Huang, G. S. Couch, D. M. Greenblatt, E. C. Meng, T. E. Ferrin, UCSF Chimera—A visualization system for exploratory research and analysis. *J. Comput. Chem.* **25**, 1605–1612 (2004).
53. X.-J. Zhang, B. W. Matthews, EDPDB: A multifunctional tool for protein structure analysis. *J. Appl. Cryst.* **28**, 624–630 (1995).
54. P. Broto, G. Moreau, C. Vandycke, Molecular structures: Perception, autocorrelation descriptor and sar studies: System of atomic contributions for the calculation of the n-octanol/water partition coefficients. *Eur. J. Med. Chem.* **19**, 71–78 (1984).
55. M. S. Laguerre, M. Saux, J. P. Dubost, A. J. P. Carpy, P. Communications, MLPP: A program for the calculation of molecular lipophilicity potential in proteins. *Pharm. Sci.* **3**, 217–222 (1997).
56. T. D. Goddard, C. C. Huang, E. C. Meng, E. F. Pettersen, G. S. Couch, J. H. Morris, T. E. Ferrin, UCSF ChimeraX: Meeting modern challenges in visualization and analysis. *Protein Sci.* **27**, 14–25 (2018).
57. J. A. Thomas, R. N. Buchsbaum, A. Zimniak, E. Racker, Intracellular pH measurements in Ehrlich ascites tumor cells utilizing spectroscopic probes generated in situ. *Biochemistry* **18**, 2210–2218 (1979).
58. W. F. Boron, P. De Weer, Intracellular pH transients in squid giant axons caused by CO<sub>2</sub>, NH<sub>3</sub>, and metabolic inhibitors. *J. Gen. Physiol.* **67**, 91–112 (1976).
59. A. Franchi, D. Perucca-Lostanlen, J. Pouyssegur, Functional expression of a human Na<sup>+</sup>/H<sup>+</sup> antiporter gene transfected into antiporter-deficient mouse L cells. *Proc. Natl. Acad. Sci. U.S.A.* **83**, 9388–9392 (1986).

**Acknowledgments:** We thank X. Huang, B. Zhu, X. Li, L. Chen, and other staff members at the Center for Biological Imaging (CBI), Core Facilities for Protein Science at the Institute of Biophysics, Chinese Academy of Science (IBP, CAS) for the support in cryo-EM data collection. We thank Y. Wu for research assistant service. **Funding:** This work was supported by the Chinese Academy of Sciences Strategic Priority Research Program (grant XDB37030304 to Y.Z. and grant XDB37030301 to X.C.Z.), the National Key Research and Development Program of China (grant 2021YFA1301501 to Y.Z.), and the National Natural Science Foundation of China (grant 92157102 to Y.Z. and grant 31971134 to X.C.Z.). We are grateful for the services provided by McGill Life Sciences Advanced BioImaging Facility and Genome Québec for DNA sequencing; platforms were supported by funding from the Canadian Foundation for Innovation. We also thank J. Hanrahan (Department of Physiology, McGill University) for providing access to the pH imaging system and funding from the Canadian Institutes of Health Research (grants PJT-155976 and PJT-166165). **Author contributions:** Y.Z. conceived the project. Y.D. carried out molecular cloning and cell biology experiments. Y.D. expressed and purified protein complex sample. Y.D. prepared sample for cryo-EM study. Y.D. and Y.G. carried out cryo-EM data collection. Y.G., H.L., and Y.Z. calculated the EM maps and plotted all figures. Y.G., H.L., and Y.Z. built and refined the atomic model. A.J., A.B., and J.O. performed AP-1 cell-based NHE3 protein expression, confocal microscope imaging, and transport assays. H.L., X.C.Z., and Y.Z. did data analysis. H.L., J.O., X.C.Z., and Y.Z. wrote the manuscript with input from all other authors. **Competing interests:** The authors declare that they have no competing interests. **Data and materials availability:** The 3D cryo-EM density map of the NHE3-CHP1 complex has been deposited in the EM Database under the accession code EMD-32971, and the coordinates for the structures have been deposited in Protein Data Bank under accession code 7X2U. All data needed to evaluate the conclusions in the paper are present in the paper and/or the Supplementary Materials.

Submitted 23 November 2021

Accepted 11 April 2022

Published 25 May 2022

10.1126/sciadv.abn3925